PHYSICAL REVIEW B **94**, 035148 (2016)

Dipole analysis of the dielectric function of color dispersive materials: Application to monoclinic Ga_2O_3

C. Sturm,[1] R. Schmidt-Grund,[1] C. Kranert,[1] J. Furthmüller,[2] F. Bechstedt,[2] and M. Grundmann[1]
[1]*Institut für Experimentelle Physik II, Universität Leipzig, Linnéstrasse 5, 04103 Leipzig, Germany*
[2]*Institut für Festkörpertheorie und -optik, Friedrich-Schiller-Universität Jena, Max-Wien-Platz 1, 07743 Jena, Germany*

(Received 2 February 2016; revised manuscript received 27 May 2016; published 22 July 2016)

We apply a generalized model for the determination and analysis of the dielectric function of optically anisotropic materials with color dispersion to phonon modes and show that it can also be generalized to excitonic polarizabilities and electronic band-band transitions. We take into account that the tensor components of the dielectric function within the Cartesian coordinate system are not independent of each other but are rather projections of the polarization of dipoles oscillating along directions defined by the, non-Cartesian, crystal symmetry and polarizability. The dielectric function is then composed of a series of oscillators pointing in different directions. The application of this model is exemplarily demonstrated for monoclinic (β-phase) Ga_2O_3 bulk single crystals. Using this model we are able to relate electronic transitions observed in the dielectric function to atomic bond directions and orbitals in the real space crystal structure. For a thin film revealing rotational domains we show that the optical biaxiality is reduced to uniaxial optical response.

DOI: 10.1103/PhysRevB.94.035148

I. INTRODUCTION

For the understanding, design, and fabrication of optoelectronic devices, the optical properties of the involved materials have to be known. A well established and powerful method for the determination of these properties is spectroscopic ellipsometry [1,2]. We concentrate here on the dielectric function (DF), which is usually obtained by means of numerical model analysis of the experimental ellipsometry data and then often described by a series of line-shape model dielectric functions in order to deduce phonon properties, free charge carrier concentrations, and the properties of electronic transitions (e.g., Refs. [2,3]). For isotropic materials this method is well established. However, in recent years, optically anisotropic materials, as, e.g., Ga_2O_3 [4–7], $CdWO_4$ [8], and lutetium oxyorthosilicate [9], went into focus of research since they are promising candidates for optoelectronic applications in the ultraviolet (UV) spectral range. However, the determination of their optical and electronic properties is more challenging compared to isotropic materials since they depend on the crystal orientation. The dielectric function is represented by a (frequency-dependent) tensor and the determination of its components requires a series of measurements for various crystal orientations.

For (nonchiral) optically anisotropic materials, the dielectric function is in general a symmetric tensor consisting of six independent components [10], i.e.,

$$\varepsilon = \begin{pmatrix} \varepsilon_{xx} & \varepsilon_{xy} & \varepsilon_{xz} \\ \varepsilon_{xy} & \varepsilon_{yy} & \varepsilon_{yz} \\ \varepsilon_{xz} & \varepsilon_{yz} & \varepsilon_{zz} \end{pmatrix}. \tag{1}$$

Due to its symmetry, this tensor can be diagonalized independently for the real and imaginary part at each wavelength separately. In the transparent spectral range, i.e., for the vanishing imaginary part, the diagonal elements are the semiprincipal axes of the ellipsoid of wave normals and are usually called dielectric axes. For materials with monoclinic or triclinic crystal structure, the orientation of the dielectric axes depends on the wavelength, an effect often called color dispersion. In the spectral range with nonvanishing absorption, the situation becomes even more complex. Due to the independent diagonalizability of the tensor (1) for the real and imaginary part, the corresponding dielectric axes in general do not coincide with each other. Thus, in general, six dielectric axes are present. For these classes of materials only a few reports on the determination of the full tensor of the DF exist, e.g., for α-PTCDA [11], pentacene [12], $BiFeO_3$ [13], $CdWO_4$ [8], $K_2Cr_2O_7$ [14], $CuSO_4 \cdot 5H_2O$ [15], and effective anisotropic materials as, e.g., slanted columnar films [16]. Most of these works are limited to the determination of the line shape of the dielectric function, treating the tensor components of the DF independently of each other. This can, from a technical point of view, result in large correlations between the individual tensor elements causing nonphysical results. More importantly, the nature of polarizabilities in the material, like phonons, excitons, and electronic band-band transitions, cannot be explored in this way. Thus, line shape model dielectric functions (MDF) representing the oscillators properties like energy, amplitude, broadening, and even oscillation direction in a meaningful and physical correct way have to be used.

Facing this, Dressel *et al.* [12] proposed an approach assuming that the dipole moments are aligned to three polarization axes which should coincide with the crystallographic axes. Taking this model into account, the tensor of the DF is fully described by its three independent principal elements and the known angles between the crystallographic axes. However, as a consequence of this approach, the principal axes of the indicatrix (related to the real part of ε) coincide with those of the conductivity tensor (related to the imaginary part of ε) which is not generally valid as shown for instance for $CdWO_4$ [8] and Ga_2O_3 [7]. To overcome this problem, Höfer *et al.* [14,15] used for the infrared spectral range a model, developed earlier by Born [17,18] for phonons and generalized by Emslie *et al.* [19], which consists of a sum of damped Lorentz oscillators individually aligned to the axis of their respective dipole moments. For phonons, these axes are related to the atomic displacement and thus to some extent to the crystallographic axes. Furthermore, their dissipative spectral range is usually narrow. Thus, the question arises if such a model can be applied to spectrally widespread excitations like electronic band-band transitions, which consist of numbers of individual dipoles whose axes are connected to overlapping atomic orbitals of various symmetry and therefore not necessarily coincide with crystallographic directions. Furthermore, the density of states (DOS) of the electronic band structure is distributed within a wide energy range in a complex manner causing nonsymmetric line shapes of the imaginary part of the dielectric function which spectrally overlap for different contributions and directions.

Here we demonstrate that the approach of oriented dipole oscillators is generally valid for all kinds of excitations. We demonstrate this exemplarily for monoclinic Ga_2O_3 (β-phase) single crystals and a thin film in the spectral range from infrared to vacuum ultraviolet. We show that this model provides a deep insight in electronic properties of the materials: Comparing the directions of the electronic polarizabilities obtained by modeling the experimental ellipsometry data using line shape MDF to the real space atomic arrangement in the crystal and considering theoretical calculated electron density distribution as well as orbital-resolved DOS allows us to assign the observed transitions to individual orbitals.

The paper is organized as follows: In Sec. II we discuss at first the general form of the DF for all kinds of crystal symmetries and its composition. After that we demonstrate its applicability to the case of β-Ga_2O_3 single crystals in the infrared and ultraviolet spectral range. Finally, we show by means of a practically relevant β-Ga_2O_3 thin film, which exhibits rotation domains, that the approach of using directed transitions explains the effective uniaxial properties of the film and enhances the sensitivity to the out-of plane component of the DF.

II. DIELECTRIC FUNCTION

In linear optics the optical response of a material is determined by dipole excitations, e.g., optical phonons, electronic band-band transitions, or excitons which in sum are represented by the dielectric function (ε). For materials with a crystal structure symmetry lower than the cubic one, the excitations generally differ in amplitude, broadening, and energy between the crystallographic directions.

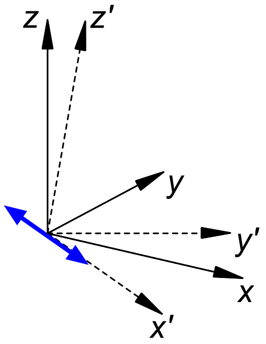

FIG. 1. Relation between the laboratory coordinate system (x, y, and z) and the system of the excitation (x', y', and z'). The blue double arrow denotes the direction of the dipole moment of the excitation as discussed in the text.

Let χ'_i be the tensor representing the susceptibility of the ith dipole excitation in the system with the principal axes given by x', y', and z' in such a way (without losing generality) that the orientation of the dipole moment coincides with the x' axis (Fig. 1). Then, the only nonzero component of χ'_i is $\chi'_{i,x'x'}$, i.e., $\chi'_{i,x'x'} \neq \chi'_{i,m'n'} = 0$ with $m',n' \in \{x',y',z'\}$. In general, the polarization direction of the excitation and the laboratory system do not coincide with each other and hence a transformation has to be performed. This transformation is typically described by means of a rotation matrix R which takes into account the Euler angles ϕ and θ. Thus the susceptibility of the ith dipole excitation in the laboratory system is given by $\chi_i = R(\phi_i,\theta_i)\chi'_i R^{-1}(\phi_i,\theta_i)$. For the entire dielectric function, the susceptibility of all excitations have to be considered, i.e.,

$$\varepsilon = \mathbb{1} + \sum_{i=1}^{N} R(\phi_i,\theta_i)\chi'_i R^{-1}(\phi_i,\theta_i). \tag{2}$$

Note, the Euler angles ϕ_i and θ_i are in general different for each excitation. The advantage of this expression is that the components of the resultant dielectric tensor in the Cartesian coordinate system are not independent of each other but rather composed of the respective projected part of the excitation's line-shape function according to the directions of their individual dipole moment. For the entire dielectric function it follows that, due to the finite broadening of each excitation and by considering Kramers-Kronig relation, the orientation of the principal tensor axes of the real and imaginary parts differ from each other as it is well known and observed in experiments, e.g., for $CdWO_4$ [8] and Ga_2O_3 [7].

Equation (2) represents the general case which has to be used for triclinic crystals. It can be simplified depending on the crystal symmetry. Crystals with monoclinic structure exhibit one symmetry axis, representing a C_2 rotation axis or the normal of a mirror plane C_s (or both, C_{2h}), which we identify in the following with the y direction. The plane perpendicular to the y axis, the x-z plane, reveals no symmetry which defines a Cartesian coordinate system preferentially. Therefore, from symmetry arguments, considering dipoles polarized either along the y axis or in the x-z plane, one can simplify Eq. (2) to

$$\varepsilon = \mathbb{1} + \sum_{i=0}^{N_y} \chi_{i,yy} + \sum_{j=0}^{N_{xz}} R(\phi_j)\chi'_j R(\phi_j)^{-1}, \tag{3}$$

with $\chi_{i,yy}$ and χ'_j being the contribution of the susceptibility of the respective directions. N_y and N_{xz} represent the number of excitations with the corresponding polarization directions and ϕ is the angle between the polarization direction and the x axes within the x-z plane. Equation (3) leads to the well known form of the DF

$$\varepsilon = \begin{pmatrix} \varepsilon_{xx} & 0 & \varepsilon_{xz} \\ 0 & \varepsilon_{yy} & 0 \\ \varepsilon_{xz} & 0 & \varepsilon_{zz} \end{pmatrix}. \tag{4}$$

A further simplification can be made for orthorhombic materials containing three orthogonal twofold rotation symmetry axes. In this case the DF can be written as

$$\varepsilon = \mathbb{1} + \sum_{i=0}^{N_x} \chi_{i,xx} + \sum_{j=0}^{N_y} \chi_{j,yy} + \sum_{k=0}^{N_z} \chi_{k,zz}, \tag{5}$$

and the dielectric function tensor contains only diagonal elements. In the case of uniaxial materials, e.g., those with a hexagonal symmetry, $\chi_{i,\mathrm{xx}} = \chi_{i,yy}$ and $N_x = N_y$ holds. For isotropic materials, the numbers of oscillators in all three directions is the same and therefore the DF reduces to the scalar given by

$$\varepsilon = 1 + \sum_{i=1}^{N} \chi_i. \tag{6}$$

For practical application Eq. (2) has to be further modified. The real and imaginary parts of any dielectric function are connected to each other by the Kramers-Kronig relations. Contributions of excitations at energies higher than the investigated spectral range to the real part of the DF have to be considered. These contributions are usually described by pole functions. In the case presented here, this means that the identity tensor in Eq. (2) has to be replaced by a real valued tensor with the form given by the corresponding crystal structure where each component is represented by a pole function.

III. EXPERIMENT

By using the approach presented in Sec. II and line-shape MDFs, the parametrized dielectric function of β-Ga_2O_3 bulk single crystals and of a thin film was determined in the mid-infrared up to the vacuum-ultraviolet spectral range by means of generalized spectroscopic ellipsometry.

Ga_2O_3 crystallizes at ambient conditions in monoclinic crystal structure, the so-called β phase (Fig. 2). The C_{2h} symmetry axis of this crystal structure coincides with the crystallographic b axis in real space and is orthogonal to the a and c axis. The angle between the nonorthogonal a and c axis is $\beta = 103.7^\circ$ [20] resulting in a nonvanishing off-diagonal element of the dielectric tensor within the Cartesian coordinate system [7,21]. We investigated two single side polished bulk single crystals from Tamura Corporation with (010) and $(\bar{2}01)$ orientation, allowing access to all components of the tensor of the DF. X-ray diffraction (XRD) measurements do not reveal any hints for the presence of rotation domains, twins, or in-plane domains.

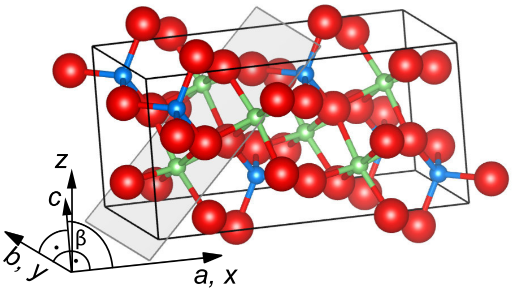

FIG. 2. Schematic representation of the unit cell of β-Ga_2O_3. The tetrahedrally coordinated Ga atoms are shown in blue, whereas the octahedrally coordinated ones are shown in green. The oxygen atoms are marked in red. The $(\bar{2}01)$ plane is highlighted by the gray rectangle. (Image created by VESTA [23].)

The thin film was deposited on a c-plane-oriented sapphire substrate by means of pulsed laser deposition (PLD) at $T \approx 730\,^\circ\mathrm{C}$. After deposition, the sample was annealed for 5 min at $T \approx 730\,^\circ\mathrm{C}$ and oxygen pressure of $p_{O_2} = 800$ mbar. XRD measurements confirm the monoclinic crystal structure of the film and the surface orientation was determined to be $(\bar{2}01)$. In contrast to the bulk single crystals, six rotation domains are observed which are rotated against each other by an angle of 60° [22]. In contrast to the bulk single crystals, which reveal a smooth surface without atomic steps, the surface roughness of the thin film was determined to be $R_s \approx 5$ nm.

For the determination of the dielectric function we use spectroscopic ellipsometry, which determines the change of the polarization state of light by interaction with a sample. In the general case, this is expressed by means of the 4×4 Mueller matrix (MM, $\mathbf{M}$) which connects the Stokes vectors of the incident (reflected) light S_{in} (S_{ref}) by $S_{\mathrm{ref}} = \mathbf{M}\, S_{\mathrm{in}}$ [1,2]. The MM can be represented as a matrix of 2×2 block matrices where the diagonal ones are mainly related to the reflection coefficients for the light polarized parallel (p) and perpendicular (s) to the plane of incidence. The off-diagonal block matrices are a measure for the conversion of s- into p-polarized light, and vice versa. In the special case where no energy transfer between orthogonal polarization eigenmodes of the probe light takes place, like for isotropic samples or optically uniaxial samples with the optical axis pointing along the surface normal (as in the case for the thin film presented here, cf. Sec. V), these block off-diagonal matrices vanishes. The change of the polarization state can then be expressed by the ratio of the complex reflection coefficients, i.e., $\rho = \tilde{r}_{\mathrm{p}}/\tilde{r}_{\mathrm{s}}$. The index represents the polarization of the light with respect to the plane of incidence.

For the determination of the DF, the experimental data are analyzed by transfer-matrix calculations considering a layer stack model taking into account the dielectric function of the involved materials [1,2]. For the bulk single crystals, the model consists of a semi-infinite substrate (Ga_2O_3 itself) and a surface layer accounting for some roughness or contaminations. For the infrared spectral range the surface layer can be neglected. For the thin film the model consists of a c-plane oriented sapphire substrate, the Ga_2O_3 thin film layer, and the surface layer. The dielectric function of sapphire was taken from the literature [24]. The surface layer was modeled using an effective medium approximation (EMA) [25] mixing the DF of Ga_2O_3 and void by 50% : 50% for the bulk single crystals [7]. For the thin film this fraction was chosen as an unknown parameter and the best match between experiment and calculated spectra was obtained for 80% : 20%. In the following we choose our coordinate system in such way that $\hat{e}_x \parallel a$ axis, $\hat{e}_y \parallel b$ axis, and $\hat{e}_z = \hat{e}_x \times \hat{e}_y$.

IV. BULK SINGLE CRYSTALS

A. Infrared spectral range

The MM in the infrared spectral range $250-1300\,\mathrm{cm}^{-1}$, corresponding to 31–161 meV, was determined at angles of

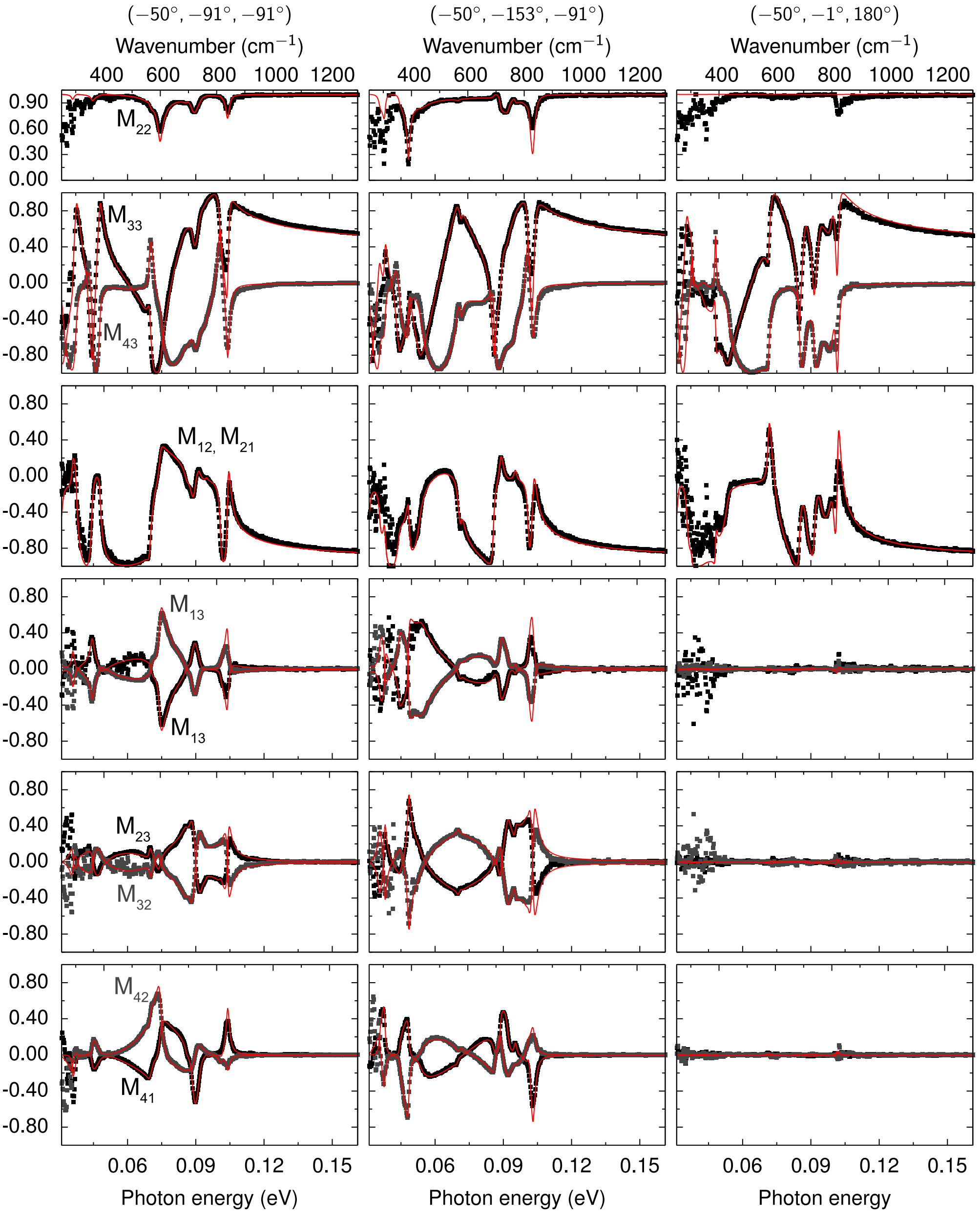

FIG. 3. Experimental (symbols) and calculated (lines) infrared spectra of the MM elements of a β-Ga$_2$O$_3$ bulk single crystal for an angle of incidence of 70°. The corresponding orientation of the crystal is given by the Euler angles on top of each column in the *yzx* notation.

incidence of 30°, 50°, and 70° for different in-plane rotations, i.e., rotating the crystal around its surface normal by 30°, 60°, and 90°. These measurements were performed using a commercial rotating compensator ellipsometer in PSCA configuration [26] with an FTIR spectrometer and a spectral resolution of 4 cm^{-1}. For selected orientations the recorded MM spectra are shown in Fig. 3. The nonvanishing block-off-diagonal elements of the MM demonstrate the optically anisotropic character of the sample.

The experimental data were modeled as described in Sec. III. The dielectric function in the infrared spectral range was described by taking into account phonons only because the contributions of free charge carriers was found to be negligible. The contribution of each phonon mode to the dielectric function is described by a Lorentz oscillator:

$$\chi'_{i,x'x'} = \frac{A_i \gamma_i E_{i,0}}{E_{i,0}^2 - E^2 - i\gamma_i E}, \tag{7}$$

with A_i, E_0, and γ being the amplitude, energy, and broadening of the ith-TO phonon mode, respectively. The entire DF is then given by Eq. (3) summing up all phonon contributions. The high energy contributions were described by a constant tensor with the shape of Eq. (4). The modeled and experimental MM spectra are shown in Fig. 3 yielding a good agreement. The parameters of the best-match MDF are summarized in Tables I and II. The obtained DF is shown in Fig. 5. Note that a similar DF is obtained by using a Kramers-Kronig consistent numerical analysis and considering the four components of the DF [Eq. (4)] to be independent of each other.

TABLE I. Experimentally determined dimensionless amplitudes (A), oscillator strength ($f_{\mathrm{expt}} = A\gamma E_0$), damping parameters ($\gamma$), and energies ($E_{0,\mathrm{expt}}$) of the TO phonon modes. The angle ϕ_{expt} represents the determined angle between the x (a) axis and the direction of the dipole moment in the x-z plane (a-c plane). The phonon energy, oscillator strength, and direction of the dipole from *ab initio* calculations are given by $E_{0,\mathrm{calc}}$, f_{calc}, and ϕ_{calc}, respectively. For comparability reasons, the experimentally determined and calculated oscillator strength was normalized to the respective values for the $B_u^{(6)}$ mode ($f^{B_u^{(6)}}$). The phonon energies taken from literature are shown in the right columns. The uncertainty of the experimentally determined data is typically 0.5 cm^{-1} for the energy, 1% for the amplitude and broadening, and 1° for the dipole orientation.

	A_{expt}	$f_{\mathrm{expt}}/f_{\mathrm{expt}}^{B_u^{(6)}}$	$f_{\mathrm{calc}}/f_{\mathrm{calc}}^{B_u^{(6)}}$	γ_{expt} (cm^{-1})	ϕ_{expt} (deg)	ϕ_{theor} (deg)	$E_{0,\mathrm{expt}}$ (cm^{-1})	$E_{0,\mathrm{calc}}$ (cm^{-1})	$E_{0,\mathrm{expt}}$ (cm^{-1})	(cm^{-1})	$E_{0,\mathrm{calc}}$ (cm^{-1})	(cm^{-1})	(cm^{-1})
$A_u^{(1)}$	–	–	0.01	–	–	–	–	160.7	155	154.8	155	155.7	141.6
$B_u^{(1)}$	–	–	0.41	–	–	101	–	224.3	250	213.7	216	202.4	187.5
$B_u^{(2)}$	–	–	0.33	8	–	176	253.5	267.3	290	262.3	300	260.4	251.6
$B_u^{(3)}$	–	–	0.03	–	–	39	–	281.9	310	279.1	337	289.7	265.3
$A_u^{(2)}$	51	0.50	0.50	21	–	–	295.3	300.5	n.o.	296.6	352	327.5	296.2
$B_u^{(4)}$	86	0.18	0.16	4	166	173	356.7	361.0	375	356.8	374	365.8	343.6
$B_u^{(5)}$	82	0.95	0.96	17	46	47	430.3	434.2	455	432.5	500	446.8	410.5
$A_u^{(3)}$	83	0.77	0.78	13	–	–	446.7	447.0	525	448.6	526	475.7	383.5
$B_u^{(6)}$	73	1.00	1.00	15	128	130	572.1	560.8	640	572.5	626	589.9	574.3
$A_u^{(4)}$	73	0.39	0.43	5	–	–	661.5	665.8	668	663.2	656	678.4	647.9
$B_u^{(7)}$	32	0.25	0.23	7	28	30	691.0	692.5	692	692.4	720	705.8	672.6
$B_u^{(8)}$	10	0.13	0.13	11	74	76	743.0	742.5	731	743.5	760	753.8	741.6
				this work					Ref. [27]	Ref. [21]	Ref. [27]	Ref. [21]	Ref. [28]

While the imaginary part of the diagonal elements is always positive, as required from causality, the off-diagonal element can be negative. This negative value does not violate any physical principles since the sign arises from the transformation of the coordinate system and depends on the orientation of the dipole moment with respect to the chosen laboratory system. Negative off-diagonal elements can also be obtained for uniaxial materials if the laboratory system does not coincide with principal axes of the tensor of the DF.

For the assignment of the symmetry of the observed optical phonon modes we have to consider their irreducible representation at the Γ point, i.e., $\Gamma = 10A_g + 5B_g + 8B_u + 4A_u$ [27]. The phonon modes with the A_g and B_g symmetry are Raman active, whereas those with A_u and B_u symmetry are infrared active. In the investigated spectral range, 9 of the total 12 infrared-active-optical phonon modes are observed. Their properties are summarized in Table I. For the modes which have a dipole moment in the x-z plane (a-c plane, B_u symmetry), the polarization direction with respect to the x (a) axis is given by the angle ϕ, which was found to differ for each phonon mode. This is also in agreement with the results recently reported by Schubert *et al.* [21]. The phonon mode $B_u^{(3)}$ was not observable in our experiment. This can be attributed to the weak sensitivity to this mode caused by its low amplitude which is predicted by *ab initio* calculations (see below) and to the pronounced noise caused by the low sensitivity of the detector of our setup in this spectral range. Furthermore, for the mode $B_u^{(2)}$ only the frequency and broadening are given since also the strong noise in this spectral range and the probable spectral overlap with $B_u^{(3)}$ prohibit the determination of its dipole direction.

For comparison we calculated the phonon modes by *ab initio* calculations based on the B3LYP hybrid functional approach implemented in the CRYSTAL14 code [29–31]. Thereby we used the Gaussian-type functions basis set of Pandey *et al.* [32] for gallium and of Valenzano *et al.* [33] for oxygen, which we slightly modified, and 150 k points in the irreducible Brillouin zone. The five tolerances T1 $\cdots$ T5 used in CRYSTAL14 to define the truncation criteria of Coulomb and exchange infinite sums were set to 8 (T1 $\cdots$ T4) and 16 (T5), respectively. Furthermore, we used a tolerance of the energy convergence of 10^{-11} Hartree. All input parameters and calculation conditions can be found in Ref. [31]. The calculated lattice parameters are $a = 1.2336$ nm, $b = 0.3078$ nm, and $c = 0.5864$ nm, in reasonable agreement with those reported in the literature [20]. The corresponding phonon mode energies, oscillator strength, and the direction of the dipoles are given in Table I and are in excellent agreement with those determined by ellipsometry [34]. The excellent agreement is not restricted to the infrared active phonon modes but is also obtained for the Raman active modes [31].

TABLE II. Contributions of the high frequency dielectric function to the dielectric tensor in the infrared spectral range.

	xx	yy	zz	xy	xy	yz
ε_∞	3.60	3.58	3.54	0.00	−0.03	0.00

B. Ultraviolet spectral range

The numeric DF in the UV spectral range, obtained by using a Kramers-Kronig consistent numerical analysis, was recently reported by us [7]. Details on the experimental setup used for this spectral range can be found in Ref. [7]. In order to extract the properties of the contributing electronic transitions, e.g., energy and electronic orbitals involved, and to demonstrate the universal applicability of Eq. (2) for electronic transitions, we analyzed the contribution of each transition to the entire DF by using line-shape model functions. Symmetry consideration and band structure properties [7,35] yield that the transitions are polarized either along the y axes or within the x-z plane. We have shown, using density functional theory calculations combined with many-body perturbation theory including quasiparticle and excitonic effects [35], that the DF in the spectral range from the fundamental absorption edge up to some eV higher is dominated by excitonic correlation effects. From these calculations we deduce that three transitions, which are polarized along the y axis and four, polarized within the x-z plane, contribute mainly to the DF in the investigated spectral range. These excitonic contributions have been described by a model function developed by Tanguy for Wannier excitons taking into account bound and unbound states [36–38]:

$$\chi_i^{\mathrm{exc}} = \frac{A_i\sqrt{E_{x,i}^{\mathrm{b}}}}{\nu_i^2}[g(\xi(\nu_i)) + g(\xi(-\nu_i)) - 2g(\xi(0))], \tag{8}$$

with

$$g(\xi) = -2f(S/\xi) - \frac{\xi}{S} - 2f(1-\xi) - \frac{1}{\xi},$$

$$\xi(x) = \frac{2}{\sqrt{\frac{E_g S - x}{E_{x,i}^{\mathrm{b}}}} + \sqrt{\frac{E_g S - x}{E_{x,i}^{b}} + \frac{4}{S}}},$$

$$f(z) = \frac{d}{dz}\ln\Gamma(z),$$

$$\nu_i = E + i\gamma_i.$$

A_i, γ_i, E_g, $E_{x,i}^{\mathrm{b}}$, and S represents the amplitude, the broadening, the energy of the fundamental bound state, the unscreened exciton binding energy, and the screening factor, which can take values between $-\infty$ (totally screened Coulomb potentials) and $+\infty$ (unscreened Coulomb potential). $\Gamma(z)$ is the Gamma function. The contribution of weakly pronounced band-band transitions were summarized by using a Gaussian oscillator (χ^{Gauss}). A further Gaussian oscillator was included to consider contributions of transitions at energies higher than the investigated spectral range due to their spectral broadening. These contributions together with the pole function (χ^{Pole}) were considered for each component of the dielectric function tensor independently because they may originate from different transitions. Thus, the dielectric function reads

$$\varepsilon = \mathbb{1} + \sum_{i=1}^{3}\chi_{i,yy}^{\mathrm{exc}} + \sum_{j=1}^{4}R(\phi_j)\chi_j'^{\mathrm{exc}}R(\phi_j)^{-1} + R(\phi_j)\chi_j'^{\mathrm{Gauss}}R(\phi_j)^{-1} + \chi^{\mathrm{high}}, \tag{9}$$

with χ^{high}:

$$\chi_{mm}^{\mathrm{high}} = \chi_{mm}^{\mathrm{Gauss}} + \chi_{mm}^{\mathrm{Pole}}, \tag{10a}$$

$$\chi_{xz}^{\mathrm{high}} = \chi_{xz}^{\mathrm{Pole}}, \tag{10b}$$

$$\chi_{xy}^{\mathrm{high}} = \chi_{yz}^{\mathrm{high}} = 0, \tag{10c}$$

and $m \in \{x,y,z\}$.

The experimentally recorded and the calculated spectra of the MM elements are shown for selected orientations in Fig. 4, yielding good agreement. The difference between the experimental and the calculated spectra for energies $E > 7$ eV was also observed by using the above mentioned numerical Kramers-Kronig-consistent analysis and might be caused by the limitation of the used approach for the description of the surface layer [7]. This can be attributed to the fact that the sensitivity to this layer is strongly enhanced in this spectral range due to the enhanced absorption and therefore reduced penetration depth of the probe light.

The parameters of the best-match MDF are summarized in Tables III and IV. We extracted a screening factor and an exciton binding energy of about $S \approx 0.7$ and $E_{\mathrm{X}}^{\mathrm{b}} = 270$ meV, respectively, for all contributions. The obtained exciton binding energy agrees well with that estimated by our theoretical calculations of $E_{\mathrm{X}}^{\mathrm{b}} = 291$ meV in the Wannier-Mott picture with an electron mass of about $0.27m_0$ and an averaged dielectric constant of $\varepsilon_\infty \approx 3.55$. The lattice polarization does not contribute to the screening because of the fact that $E_{\mathrm{X}}^{\mathrm{b}}$ is much larger than the highest optical phonon frequency. That means the lattice is not fast enough to contribute to the electron-hole screening [39]. Note that we considered the same exciton binding energy for all excitonic transitions because of the strong correlation between energy of the fundamental bound state and the corresponding binding energy. This assumption is further supported by the fact that the upper valence bands are rather flat with large hole masses, so that the binding energy of all excitons is ruled by the electron mass, i.e., the dispersion of the lowest conduction band at the Γ point which is nearly isotropic.

The dispersion of the tensor elements for the entire investigated spectral range is shown in Fig. 5. The contributions of excitonic transitions to ε_2 are shown as colored solid lines (from red to blue). The orientation of the corresponding dipole moments in the x-z plane is indicated by the arrows in the inset. In agreement with our theoretical calculations and the numeric MDF [7,35], the two energetically lowest transitions (labeled as X_1 and X_2) are strongly polarized along the x and z direction, respectively. At higher energies, there are transitions along the y axis (b axis, labeled as X_i^b) and within the x-z plane (a-c plane, labeled as X_3 and X_4). The directions of the dipole moments of the excitonic transitions ($X_1 \cdots X_4$) in the x-z plane with respect to the x axis are denoted by the angle ϕ (Table III). Our band structure calculations (for details see Ref. [35]) reveal also that for light polarized in the x-z plane the absorption is dominated by four transitions. The direction of their corresponding transition dipoles is in excellent agreement with those obtained by ellipsometry. This indicates that the excitons are mainly formed by these individual band-band transitions.

Based on calculated charge distribution [40] and atomic arrangement within the x-z plane (a-c plane), we relate the directions of the dipole moments of all four pronounced excitonic excitations within this plane ($X_1 \cdots X_4$), obtained from the ellipsometry model, to atomic bonds in the crystal structure as shown in Fig. 6. For transitions along the y axis, no direct assignment to individual orbitals was possible because of the

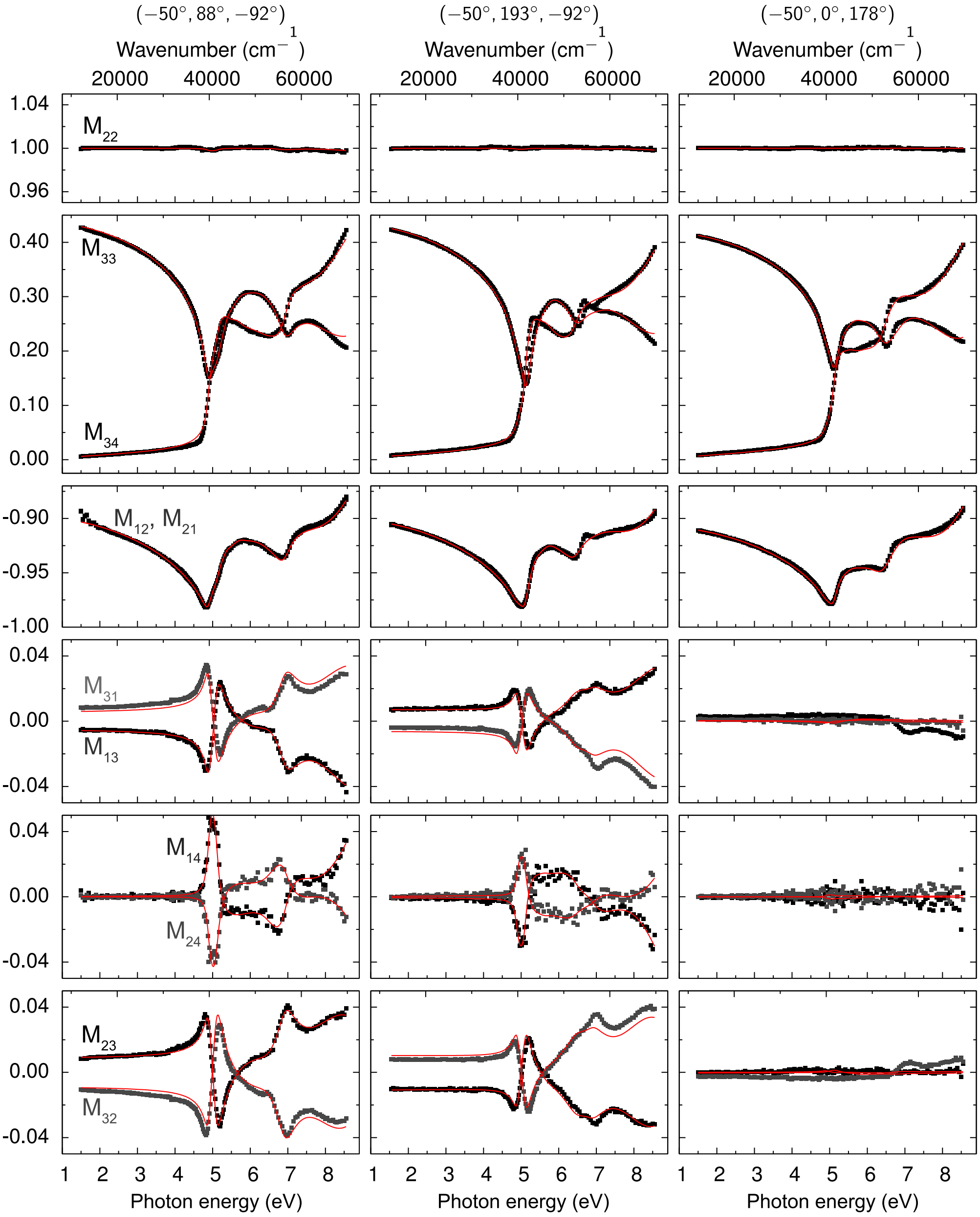

FIG. 4. Experimental (symbols) and calculated (lines) spectra of the MM elements of a β-Ga$_2$O$_3$ bulk single crystal for an angle of incidence of 70°. The corresponding orientation of the crystal is given by the Euler angles on top of each column in the yzx notation.

complex distribution of atomic bonds. Please note that the uncertainty in the experimentally determined dipole moment directions amounts to 10°, caused by the simplification due to the used model functions, which summarize spectrally over different individual transitions. As all these transitions reveal no contribution to ε_{yy}, only bonds located solely within the subplanes of the x-z plane (a-c plane) are considered (cf. Fig. 6). It is found that all excitonic transitions except the first one, which appears to take place between oxygen atoms, are between differently coordinated gallium and oxygen. In the following discussion we will use the nomenclature given by Geller [20] and label the tetrahedrally and octahedrally coordinated Ga atoms as Ga(I) and Ga(II), respectively, while the three different sites of the oxygen atoms are labeled as O(I), O(II), and (OIII). These atoms are located in the plane perpendicular to the C_2 rotation axis (b axis) and on five sets of the Wyckoff position 4i, i.e., $(000,\frac{1}{2}\frac{1}{2}\frac{1}{2}) \pm (x0z)$ (cf. Fig. 6) [20].

Band structure calculations reveal that the uppermost valence bands are dominated by oxygen p orbitals, while the DOS of the lowest conduction bands is composed of almost equal contributions from Ga s, O s, and O p orbitals [5,35,40,41]. Thus, dipole allowed transitions can take place from O p orbitals to Ga s and O s orbitals. It turns out that the states near the conduction band minimum are preferentially determined by octahedrally coordinated Ga(II) [40]. This is reflected by the assignment of the dipole directions to the atomic bonds in Fig. 6. The transition X_2, almost directed along the x (a) axis, involves O and Ga(II) and also reveals a high amplitude in the DF. Ga(II) is located between O(II) and O(III). The best match of the experimentally determined as well as

TABLE III. Parameters of the UV model dielectric functions for the observed transitions within the investigated spectral range. The angle ϕ represents the determined orientation of the dipole moment in the x-z plane (a-c plane) with respect to the x (a) axis. Right columns: The calculated lowest allowed quasiparticle transitions for the uppermost valence bands into the lowest conduction band at the Γ point (only allowed transitions are given). The number of the valence band is given by VB. The quasiparticle energies E_{calc} has to be shifted by about 0.2 eV toward lower energies to approach the measured exciton energies. The optical transition strengths are characterized by the squares of the Cartesian components of the velocity operator v_i and the resulting dipole orientation is given by ϕ_{calc}. The uncertainty of the experimentally determined data are up to 20 meV for the energy, 10% for the amplitudes and broadening, and 10° for the dipole orientation.

			Experiment					Calculation				
Label	Direction	Type	A_{expt} (eV$^{3/2}$)	E_{expt} (eV)	γ_{expt} (meV)	ϕ_{expt} (deg)	VB	E_{calc} (eV)	v_x ($m\hbar/a_{\mathrm{B}}$)	v_y ($m\hbar/a_{\mathrm{B}}$)	v_z ($m\hbar/a_{\mathrm{B}}$)	ϕ_{calc} (deg)
X_1	a-c	Exciton	15	4.88	70	110	44	5.05	–0.15	0.00	0.39	110.8
X_2	a-c	Exciton	18	5.10	80	17	43	5.29	0.43	0.00	0.14	17.7
X_3	a-c	Exciton	16	6.42	215	48	38	6.75	0.12	0.00	0.24	62.9
X_4	a-c	Exciton	26	6.90	170	119	34	7.33	–0.17	0.00	0.20	130.2
G_1	a-c	Gauss	0.28	6.08	1.378	124	–	–	–	–	–	–
X_1^b	b	Exciton	8.3	5.41	75	–	41	5.62	0.00	0.23	0.00	–
X_2^b	b	Exciton	20	5.75	139	–	39	5.99	0.00	0.46	0.00	–
X_3^b	b	Exciton	3.5	6.87	253	–	32	7.95	0.00	0.02	0.00	–

calculated dipole orientation is obtained for the Ga(II)-O(III) bond, indicating that the transition X_2 is mainly related to the orbitals of this bond. The transitions X_3 and X_4 are assigned to take place between Ga(I) and O(III). The directions obtained from model analysis of the DF does not fit as good as for transition X_2, may be caused in correlation effects due to spectral overlap of different contributions to the DF. Finally, transition X_1, directed almost along the crystallographic c axis, was assigned to take place either between O(I) and O(III) or between two O(II) atoms, or both. While the first possibility involves differently coordinated atoms suggesting dipole allowed transitions between p- and s-like orbitals, the second possibility involves similar coordinated atoms (s-like character) which implies a lower oscillator strength. The relatively high amplitude of this transition is not fully understood, because based on our calculations [35] and Ref. [40], the charge density between the involved atoms and also the DOS of the oxygen orbitals in the conduction band is predicted to be relatively low.

These results nicely demonstrate the potential of the used model approach for the tensor of the dielectric function to gain deep insight into electronic properties of highly anisotropic materials.

TABLE IV. Parameters of the UV model dielectric function describing the contributions of the high energy transition to the dielectric function in the investigated spectral range.

	Gauss			Pole	
	A	E (eV)	γ (eV)	A (eV^2)	E (eV)
$\chi_{xx}^{\mathrm{high}}$	1.41	9.18	2.5	138	11.9
$\chi_{yy}^{\mathrm{high}}$	1.47	8.89	2.8	154	11.8
$\chi_{zz}^{\mathrm{high}}$	1.97	8.97	1.7	105	11.7
$\chi_{xz}^{\mathrm{high}}$	–	–	–	36.3	20.4

V. THIN FILM

As mentioned above, the PLD-grown β-Ga$_2$O$_3$ thin film exhibits ($\bar{2}01$) out-of-plane orientation with six in-plane rotation domains, rotated by multiples of 60°. As their size is much smaller than the optically probed sample area of about 5×8 mm^2, the measured optical response is determined by an average over these domains. Thus, this film can be described as an effective medium [2]. Assuming an uniform distribution of these rotation domains, the dielectric function of this effective material is given by

$$\varepsilon = \frac{1}{6}\sum_{k=1}^{6} R(\theta_k)\varepsilon^{\mathrm{mono}}R^{-1}(\theta_k) = \begin{pmatrix} 0.5(\tilde{\varepsilon}_{xx}+\tilde{\varepsilon}_{yy}) & 0 & 0 \\ 0 & 0.5(\tilde{\varepsilon}_{xx}+\tilde{\varepsilon}_{yy}) & 0 \\ 0 & 0 & \tilde{\varepsilon}_{zz} \end{pmatrix}, \tag{11}$$

with $\varepsilon^{\mathrm{mono}}$ being the dielectric tensor of one rotation domain which has a shape given by Eq. (4), $\theta_k = (k-1)\pi/3$ being the rotation angle of the kth rotation domain ($k = 1,\ldots,6$), and $R(\theta_k)$ is the rotation matrix around the surface normal. The components $\tilde{\varepsilon}_{mm}$ ($m \in \{x,y,z\}$) are defined in such a way that $\tilde{\varepsilon}_{xx}$ and $\tilde{\varepsilon}_{yy}$ are the contributions perpendicular, whereas $\tilde{\varepsilon}_{zz}$ is the contribution along the sample surface normal. Taking into account Eq. (3), the tensor elements are

$$\tilde{\varepsilon}_{xx} = 1 + \sum_j \chi'_{j,x'x'}\cos^2(\phi_j+\phi_0), \tag{12a}$$

$$\tilde{\varepsilon}_{yy} = 1 + \sum_i \chi_{i,yy}, \tag{12b}$$

$$\tilde{\varepsilon}_{zz} = 1 + \sum_j \chi'_{j,x'x'}\sin^2(\phi_j+\phi_0), \tag{12c}$$

with $\chi'_{x'x'}$ and χ_{yy} being, as described in Sec. II, the susceptibility of the jth and ith excitation in the x-z plane and along the y direction, respectively. The angle ϕ_j represents the orientation of the dipole moment of the jth excitation with

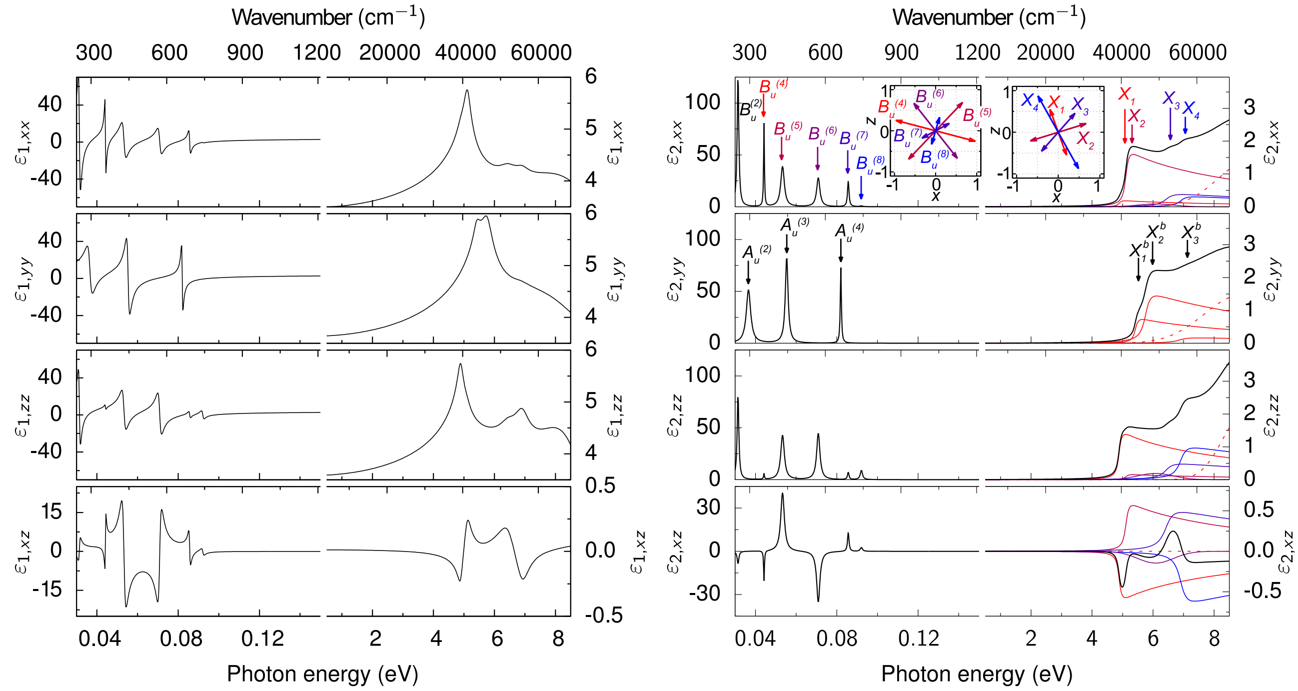

FIG. 5. Dielectric function (black solid line) of a β-Ga$_2$O$_3$ bulk single crystal in the infrared and UV spectral range. The red to blue colored solid lines represent the contribution in the investigated UV spectral range, whereas the red dashed lines represent the contribution of the high-energy contributions. The arrows in the insets depict the orientation of the corresponding dipole moments of the phonons and the excitonic transitions in the x-z plane (a-c plane) and their relative amplitude ratio.

respect to the x (a) axis and $\phi_0 = 40.1^\circ$ the angle between the surface plane and the x (a) axis.

Equation (11) is similar to those of an uniaxial material. Thus the film can be treated as optically uniaxial with $\varepsilon_\perp = 0.5(\tilde{\varepsilon}_{xx} + \tilde{\varepsilon}_{yy})$ and $\varepsilon_\parallel = \tilde{\varepsilon}_{zz}$ ($\perp$ and $\parallel$: perpendicular and parallel to the optical axis) with an orientation of the effective optical axis along the surface normal.

For such samples the sensitivity to $\varepsilon_\parallel$ is usually limited [42] due to the high index of refraction of the investigated material resulting in a propagation direction of the wave within the sample with only very small angles off the optical axis. But there is a finite projection of the electromagnetic field strength onto the optical axis and thus the optical response is determined by $\varepsilon_\perp$ and $\varepsilon_\parallel$ in any case, which have to be considered in order to obtain a physical meaningful dielectric function [43]. However, in contrast to a homogeneous uniaxial material, those effective $\varepsilon_\perp$ and $\varepsilon_\parallel$ are not independent of each other. It is obvious from Eqs. (11) and (12) that the

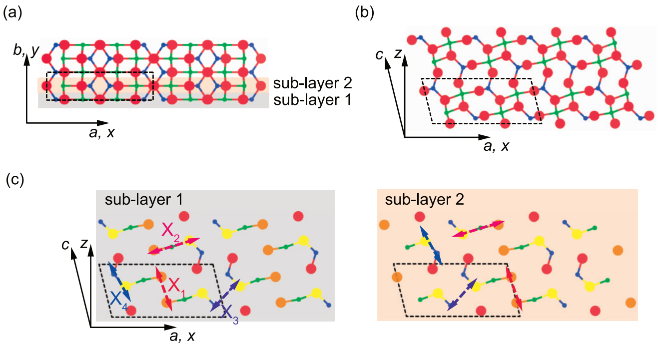

FIG. 6. (a) and (b) Schematic representation of projections of the crystal structure of β-Ga$_2$O$_3$ into the x-y plane (a-b plane) (a) and x-z plane (a-c plane) (b). The unit cell is indicated by the black framed box. Bonds are indicated by lines between the atoms. The tetrahedrally coordinated Ga(I) atoms are shown in blue and the octahedrally coordinated Ga(II) are shown in green. The oxygen atoms are marked in red. (c) Sublayers of the x-z plane (a-c plane) (left: sublayer 1, right: sublayer 2) as indicated in (a). Here the oxygen atoms at different lattice sites are highlighted by colors as O(I) red, O(II) orange, and O(III) yellow (see also text). The dashed colored arrows relate the dipole directions of the transitions $X_1 \cdots X_4$ to atomic bonds within the crystal structure. Please note that only one example is shown for each transition. (Images created by VESTA [23].)

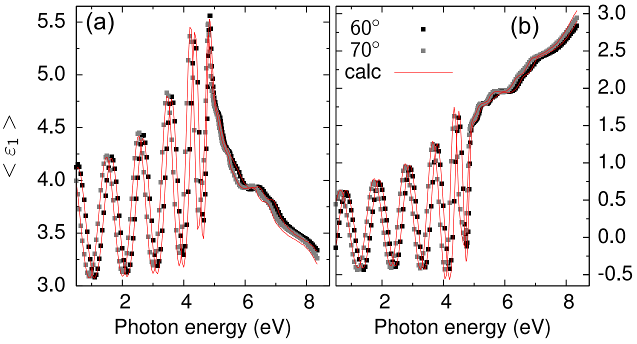

FIG. 7. Real (a) and imaginary (b) part of the thin film's pseudodielectric function for angles of incidence 60° and 70°. The experimental and calculated data are shown as symbols and red solid lines, respectively.

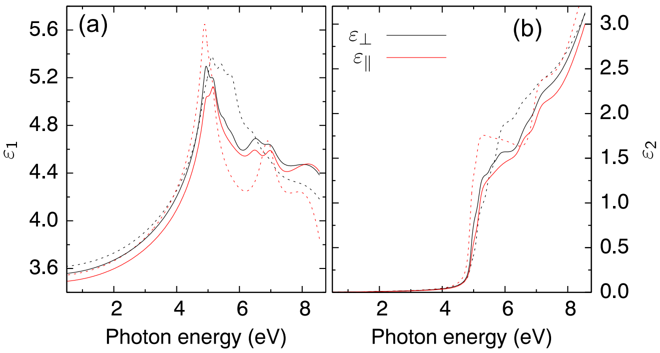

FIG. 8. Real (a) and imaginary (b) part of the tensor components of the Ga_2O_3 thin film (solid lines). For comparison, the components calculated by Eq. (11) using the single crystal values are shown as dashed lines.

same transitions contribute to both $\tilde{\varepsilon}_{xx}$ and $\tilde{\varepsilon}_{zz}$. Thus, the transitions contributing to $\varepsilon_\parallel$ appear also in $\varepsilon_\perp$ which differ only in the ratio of the corresponding oscillator strength (f) by $f_{i,zz}/f_{i,xx} = \sin^2(\phi_i + \phi_0)/\cos^2(\phi_i + \phi_0)$. Note, the opposite is not valid, since transitions contributing to $\tilde{\varepsilon}_{yy}$ and therewith also to $\varepsilon_\perp$ do not appear in $\varepsilon_\parallel$. Compared to homogeneous uniaxial materials, this correlation results in more sensitivity for the determination of the tensor component $\varepsilon_\parallel$.

The uniaxial behavior of the film with the optical axis parallel to the surface normal is reflected by vanishing off-diagonal elements of the MM. Therefore, standard ellipsometry is sufficient for measuring the full optical response (cf. Sec. III). The experimental data are shown in Fig. 7 in terms of the pseudodielectric function [2]

$$\langle\varepsilon\rangle = \langle\varepsilon_1\rangle + i\langle\varepsilon_2\rangle = \sin^2\Phi\left[1 + \tan^2\Phi\left(\frac{1-\rho}{1+\rho}\right)^2\right], \quad (13)$$

with Φ being the angle of incidence. Below $E \approx 4.8$ eV, oscillations due to multiple reflection interferences caused by the interfaces within the sample are observed which vanish with the onset of the absorption at higher energies. These interferences allows a precise determination of the thickness of the thin film which is about 330 nm.

For the parametric model of the dielectric function of the thin film we used the same set of model dielectric functions as for the bulk single crystal. The calculated spectra are shown as red solid lines in Fig. 7 and a good agreement between the experimental and calculated data is apparent. The tensor components of the dielectric function of the thin film are shown in Fig. 8. For comparison, the components calculated from the DF of the bulk single crystal by using Eq. (11) are shown as dashed lines. For the thin film, we needed to adjust energies and amplitudes of the transitions and even the dipoles' orientation angles ϕ within the x-z plane (a-c plane). The other parameters, e.g., broadening and exciton binding energy, were kept constant and were taken from the bulk single crystal model DF in order to reduce the parameter correlation. Compared to the DF of the single crystal, a blue shift of the transition energies and a lowering of the oscillator strengths is observed for the thin film. The reduced oscillator strength in the investigated spectral range cannot explain the lowering of the real part of the dielectric constant and therewith of the index of refraction in the visible spectral range only. Therefore, the reduced refractive index indicates also a reduced oscillator strength of the high energy transitions compared to the bulk single crystal. We relate these changes of the DF properties compared to the bulk single crystal on the one hand to crystal imperfections typically lowering the oscillator strength of electronic transitions by dissipative processes. On the other hand, also strain will be possibly present in the thin film, causing changes in the bond length and maybe also torsion of the unit cell causing different dipole moment orientations.

VI. SUMMARY

We have determined the dielectric function of β-Ga_2O_3 by using a generalized oscillator model taking into account the direction of the dipole moments for each transition. Within this model, the components of the tensor of the dielectric function within the Cartesian coordinate system are not independent of each other but are determined by the projection of the corresponding dipole direction. In doing so, we could determine the tensor components of the DF of β-Ga_2O_3 bulk single crystals and a thin film. By means of the determined direction of the dipoles we assign the involved orbitals for the observed transitions. For the thin film we showed that the presence of rotation domains leads to the formation of an effective uniaxial material. The sensitivity to the out-of-plane component of the dielectric function is enhanced compared to pure uniaxial materials since it is connected to the in-plane component. This allows a precise determination of this component even if the optical axis is perpendicular to the surface, which is relevant for applications in optoelectronics.

ACKNOWLEDGMENTS

We thank Hannes Krauß, Vitaly Zviagin, and Steffen Richter for the support of the ellipsometry measurements. This work was supported by the Deutsche Forschungsgemeinschaft within Sonderforschungsbereich 762 - "Functionality of Oxide Interfaces." We also acknowledge financial support of the Austrian Fond zur Förderung der Wissenschaftlichen Forschung in the framework of SFB25 - "Infrared Optical Nanostructures."

---

[1] R. Azzam and N. Bashara, *Ellipsometry and Polarized Light* (North-Holland, Amsterdam, 1977).
[2] H. Fujiwara, *Spectroscopic Ellipsometry: Principles and Applications*, 1st ed. (John Wiley and Sons, New York, 2007).
[3] M. Schubert, *Infrared Ellipsometry on Semiconductor Layer Structures: Phonons, Plasmons, and Polaritons*, Springer Tracts in Modern Physics (Springer, Berlin, 2004).

[4] N. Ueda, H. Hosono, R. Waseda, and H. Kawazoe, Appl. Phys. Lett. **71**, 933 (1997).

[5] K. Yamaguchi, Solid State Commun. **131**, 739 (2004).

[6] J. B. Varley and A. Schleife, Semicond. Sci. Technol. **30**, 024010 (2015).

[7] C. Sturm, J. Furthmüller, F. Bechstedt, R. Schmidt-Grund, and M. Grundmann, APL Mater. **3**, 106106 (2015).

[8] G. E. Jellison, M. A. McGuire, L. A. Boatner, J. D. Budai, E. D. Specht, and D. J. Singh, Phys. Rev. B **84**, 195439 (2011).

[9] G. E. Jellison, E. D. Specht, L. A. Boatner, D. J. Singh, and C. L. Melcher, J. Appl. Phys. **112**, 063524 (2012).

[10] M. Born and E. Wolf, *Principles of Optics: Electromagnetic Theory of Propagation, Interference and Diffraction of Light*, 7th ed. (Cambridge University Press, Cambridge, 1999).

[11] M. Alonso, M. Garriga, N. Karl, J. Ossó, and F. Schreiber, Organ. Electron. **3**, 23 (2002).

[12] M. Dressel, B. Gompf, D. Faltermeier, A. K. Tripathi, J. Pflaum, and M. Schubert, Opt. Express **16**, 19770 (2008).

[13] D. Schmidt, L. You, X. Chi, J. Wang, and A. Rusydi, Phys. Rev. B **92**, 075310 (2015).

[14] S. Höfer, J. Popp, and T. G. Mayerhöfer, Vib. Spectrosc. **72**, 111 (2014).

[15] S. Höfer, J. Popp, and T. G. Mayerhöfer, Vib. Spectrosc. **67**, 44 (2013).

[16] D. Schmidt and M. Schubert, J. Appl. Phys. **114**, 083510 (2013).

[17] M. Born, *Dynamik der Kristallgitter* (B. G. Teubner, Berlin, 1915).

[18] M. Born and K. Huang, *Dynamical Theory of Crystal Lattices* (Oxford University Press, Oxford, 1956).

[19] A. G. Emslie and J. R. Aronson, J. Opt. Soc. Am. **73**, 916 (1983).

[20] S. Geller, J. Chem. Phys. **33**, 676 (1960).

[21] M. Schubert, R. Korlacki, S. Knight, T. Hofmann, S. Schöche, V. Darakchieva, E. Janzén, B. Monemar, D. Gogova, Q.-T. Thieu, R. Togashi, H. Murakami, Y. Kumagai, K. Goto, A. Kuramata, S. Yamakoshi, and M. Higashiwaki, Phys. Rev. B **93**, 125209 (2016).

[22] D. Splith, S. Müller, F. Schmidt, H. von Wenckstern, J. J. van Rensburg, W. E. Meyer, and M. Grundmann, Phys. Status Solidi (a) **211**, 40 (2014).

[23] K. Momma and F. Izumi, J. Appl. Crystallogr. **44**, 1272 (2011).

[24] D. P. H. Yao and C. H. Yan, J. Appl. Phys. **85**, 6717 (1999).

[25] D. A. G. Bruggeman, Ann. Phys. **416**, 636 (1935).

[26] PSCA stands for polarizer - sample - compensator - analyzer.

[27] D. Dohy, G. Lucazeau, and A. Revcolevschi, J. Solid State Chem. **45**, 180 (1982).

[28] B. Liu, M. Gu, and X. Liu, Appl. Phys. Lett. **91**, 172102 (2007).

[29] R. Dovesi, R. Orlando, A. Erba, C. M. Zicovich-Wilson, B. Civalleri, S. Casassa, L. Maschio, M. Ferrabone, M. D. L. Pierre, P. D'Arco, Y. Noel, M. Causa, M. Rerat, and B. Kirtman, Int. J. Quantum Chem. **114**, 1287 (2014).

[30] R. Dovesi, V. R. Saunders, C. Roetti, R. Orlando, C. M. Zicovich-Wilson, F. Pascale, B. Civalleri, K. Doll, N. M. Harrison, I. J. Bush, P. D'Arco, M. Llunell, M. Causà, and Y. Noël, *CRYSTAL14 User's Manual* (University of Torino, Torino, 2014).

[31] C. Kranert, C. Sturm, R. Schmidt-Grund, and M. Grundmann, arXiv:1606.07409.

[32] R. Pandey, J. E. Jaffe, and N. M. Harrison, J. Phys. Chem. Solids **55**, 1357 (1994).

[33] L. Valenzano, F. J. Torres, K. Doll, F. Pascale, C. M. Zicovich-Wilson, and R. Dovesi, Z. Phys. Chem. **220**, 893 (2006).

[34] The Coulomb interaction is taking into account in our calculations and is reflected by the calculated oscillator strength which is also a measure for the TO-LO splitting.

[35] J. Furthmüller and F. Bechstedt, Phys. Rev. B **93**, 115204 (2016).

[36] C. Tanguy, Phys. Rev. Lett. **75**, 4090 (1995).

[37] C. Tanguy, Phys. Rev. Lett. **76**, 716 (1996).

[38] C. Tanguy, Phys. Rev. B **60**, 10660 (1999).

[39] F. Bechstedt, *Many-Body Approach to Electronic Excitations: Concepts and Applications*, Springer Series in Solid-State Sciences, Vol. 181 (Springer, Berlin, 2015).

[40] F. Litimein, D. Rached, R. Khenata, and H. Baltache, J. Alloys Compd. **488**, 148 (2009).

[41] H. He, M. a. Blanco, and R. Pandey, Appl. Phys. Lett. **88**, 261904 (2006).

[42] P. Drude, Ann. Phys. **272**, 865 (1889).

[43] S. Shokhovets, L. Spieß, and G. Gobsch, J. Appl. Phys. **107**, 023509 (2010).